Catalysis Today 405-406 (2022) 2–13

Contents lists available at ScienceDirect

Catalysis Today

journal homepage: www.elsevier.com/locate/cattod

# FIB-SEM tomography in catalysis and electrochemistry☆

Tania Rodenas, Gonzalo Prieto *

*ITQ Instituto de Tecnología Química, Universitat Politècnica de València-Consejo Superior de Investigaciones Científicas (UPV-CSIC), Av. Los Naranjos s/n, 46022 Valencia, Spain*

ARTICLE INFO

*Keywords:*
Catalysts
3D imaging
Pore tortuosity
Pore constrictivity
Three phase boundary
Hierarchically porous materials

ABSTRACT

Tomographic imaging methods have been incorporated, mostly from other scientific disciplines, into catalysis research. They are invaluable tools for the structural diagnostics of solid catalyst and electrode materials, which uniquely provide information on notions of spatial character which remain out of reach for conventional single-projection, i.e. 2D, microscopy methods. Focused-Ion-Beam Scanning-Electron-Microscopy (FIB-SEM) tomography is a destructive, slicing-type tomographic method which offers spatial resolutions down to few nm for inspection volumes up to several tens of μm across. As such, it has attracted a significant deal of attention as a means to study mesoscale features and macropore networks in catalytic materials. In this review, we first provide a succinct account on the recent technical developments in dual-beam technologies and discuss their implications for tomographic imaging experiments. Next, an exemplary experimental workflow for FIB-SEM experiments is discussed, with emphasis on technical aspects which concern specifically work with highly porous, electrically insulating catalyst materials. Contributions of FIB-SEM tomography to the quantification of mass transport-relevant topological parameters in porous catalysts, and multiple-phase boundaries of significance for concomitant mass and charge transport phenomena in electrode materials are surveyed. The application of FIB-SEM tomography for the analysis and rational development of materials in catalysis and electrochemistry has seen a fast surge over the last decade. It promises to continue consolidating as an important diagnostic tool for meso- and nano-spatial structural features, e.g. in multi-functional composite catalyst materials, wherein the relative spatial location of different sub-materials/functionalities are determinant for performance.

## 1. Introduction

Advances in the precision diagnostics and deliberate control of the structure of functional solids, at various lengthscales from the atomic level through the nano-, micro- and meso-scales, are central to developments in catalysis and related technologies. A plethora of physicochemical techniques are available to catalysis scholars and technologists which offer valuable structural and chemical information [1]. However, this information is typically subjected to a "mean-field" averaging over the entire amount of sample probed. Complementary, microscopy methods deliver spatially resolved structural insights, and have therefore become an essential instrument in the catalyst design toolbox.

Conventional microscopy methods rely on projections of the irradiated specimen on a single plane, e.g. an X-ray or a transmission-electron micrograph. This holds so even for methods like scanning-electron microscopy, which detect secondary electrons emitted during the raster-scanning of the surface of solid specimens, and thus retain a certain sense of shape and depth in the resulting 2D micrographs. The projection effect erases information and makes it essentially impossible to evaluate structural features which are spatial in nature. These include parameters of prominent significance for the functionality of catalysts, such as the location and spacing between different (active) species, the extension of interfaces between various active and/or coadjuvant phases, or higher order topology parameters in porous architectures, such as pore connectivity, pore tortuosity, pore constrictivity, etc, which are of significance for the kinetics of pore mass transport processes.

To fill this information gap, tomographic (3D) imaging methods have been introduced into the toolkit of catalysis research, in most cases after being developed in other scientific disciplines such as life- and geosciences. Fig. 1a schematically summarizes different tomographic methods, which are increasingly applied in catalysis research, organized as a function of their spatial resolution and the volume of material which may be imaged in a single experiment.

Although not a microscopy strict sense, atom-probe tomography

☆ Invited contribution to Special Issue: Nanoporous materials for energy in new era of carbon emission and carbon neutral

* Corresponding author.
*E-mail address:* prieto@itq.upv.es (G. Prieto).

https://doi.org/10.1016/j.cattod.2022.09.013
Received 24 April 2022; Received in revised form 12 September 2022; Accepted 21 September 2022
Available online 23 September 2022

(ATP) delivers information on 3D element distributions with near-atomic resolution, which is instrumental e.g. to assess spatial patterns in bi- and multi-metallic catalysts [2,3]. Electron microscopy, sometimes referred to as 3D TEM, covers the sub-10 nm resolution regime for nanosized specimens and has proven informative to assess the shape of metal nanoparticles [4,5], their nanospatial distribution and spacing when supported on porous carriers [6–9], as well as the topology of mesopore networks [10]. X-ray tomography delivers information on micrometer sized features, e.g. large pore channels or voids in technical catalyst bodies, micromonoliths and electrode materials [11–13]. More recently, ptychographic imaging with electron beams (electron ptychography, in scanning-transmission electron microscopes) [14] and high coherence X-ray beams (X-ray ptychography, at synchrotron facilities)[15–17] have demonstrated possibilities to overcome the restrictive interrelations between spatial resolution and the volume of specimen imaged at once. Ptychographic methods rely, experimentally, on the detection of a vast number of diffraction patterns as an e- or X-ray-beam probe scans the specimen. Reconstruction is computational, through a coherent diffraction imaging (CDI) analysis of interference between diffraction patterns from partially overlapping sub-volumes, and it offers possibilities for wavelength-limited spatial resolution.

Effectively bridging the nanoscale and microscale regimes, focused-ion-beam scanning electron microscopy (FIB-SEM) tomography, sometimes referred to as *FIB nanotomography*, offers spatial resolutions from few to hundreds of nm for inspected volumes of up to tens of μm lateral sizes [18]. Originating in the area of semiconductor material science, this destructive (physical slicing) tomographic method started to be applied in catalysis-related research about 15 years ago. It has since spurred, particularly over the last decade, a steadily increasing interest among the catalysis scientific community (Fig. 1b). The combination of volumetric sampling and spatial resolution offered by FIB-SEM tomography makes it particularly suitable to access topological information from complex macroporous networks, which are ubiquitous — and actually a central design playground — in (electro)catalytic applications wherein pore transport phenomena are influential for the overall performance.

It is the aim of this review to, firstly, provide a succinct view over the technical state-of-the-art and experimental workflow of FIB-SEM tomography, with emphasis on its application to study catalyst materials. Next, the potential of this technique in the areas of catalysis and electrochemical technologies is illustrated with showcase examples from the scientific literature. Finally, an outlook is presented how the scope of this tomographic technique may expand across catalysis research.

## 2. FIB-SEM systems: technical developments and state-of-the-art

Focused-Ion-Beam (FIB) methods originate from the semiconductors material science and technology in the late 1970 s [19]. The system uses a beam of ions which, unlike conventional projection ion beam systems, is finely focused into a nm-thick probe which can scan on solid samples according to pre-established spatio-temporal patterns. FIB offer unsurpassed capabilities for the removal (milling) and deposition of matter from/on solids with down to ca. 5–10 nm precision. They are typically integrated with the imaging capabilities of SEM utilities in a single platform, in so-called dual-beam or cross-beam instruments [18,20]. In these systems, the optical axes of a FIB ion gun and a SEM e-gun converge at a point in space, on the surface of the solid specimen, forming an angle which depends on the manufacturer, but it is typically in the range of 52–55 degree. This configuration enables a synchronized FIB erosion of nm-thin slices of material, followed by sequential SEM imaging of the freshly exposed material's cross-sections, with high-spatial fidelity. This is the technical basis of FIB-SEM tomography.

The interaction of FIB with the surface of solid specimens in a vacuum chamber (ca. $10^{-7}$ mbar) brings about a collection of both elastic and inelastic collision events. If the kinetic energy delivered by the ions in the FIB exceeds the binding energy in the solid specimen, the collision may cause the target atoms within the latter to be displaced from their lattice positions and ejected as sputtered particles from the surface of the material. Often, matter ejected from the specimen into the gas phase, at the point of contact with the FIB, is not in gas-phase thermodynamic equilibrium and thus, tends to condense back (re-deposit) onto nearby areas on the sample. Besides erosion (milling), implantation of ions from the FIB into the lattice of the specimen material, and local amorphization of crystalline samples, may also be observed on exposure to the ion beam.

With regard to the FIB gun, liquid metal ion sources (LMIS), prototypically based on gallium, have been the most widespread over the last decades. Usually, the ion source consists of a reservoir of liquid Ga metal ($T_{melt}$=303 K) which feeds into an acute tungsten needle. These ion sources have long proven to be robust, and provide high brilliance, often ~$10^6$ A cm$^{-2}$ sr at a maximum beam current of about 100 nA. However, implantation of Ga atoms on the specimen is commonly observed, particularly in inorganic materials such as those of prevalent interest in catalysis. More recently, gaseous ion sources (GIS) have started to proliferate as an alternative to LMIS [21]. Based on ions of much lighter elements, such as He, Ne, O or N, GIS reduce the undesired ion implantation and sample amorphization effects significantly. Besides, they

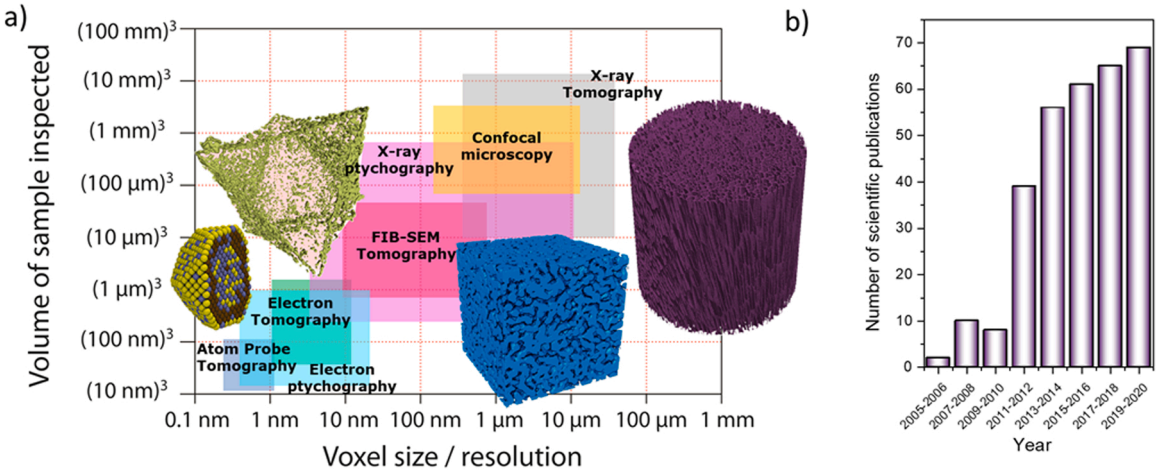


**Fig. 1.** a) Classification of various tomographic imaging methods, of significance for research in catalysis, according to their spatial resolution and their volumetric sampling capacity. b) Evolution of the number of scientific publications applying FIB-SEM tomography for investigations in the area of (electro)catalysis.
(a) The illustration for Atom Probe Tomography is adapted from [77]. (b) Data retrieved from the Scopus searcher using " catalysis " or " electrode " and " FIB-SEM tomography " or " FIB nanotomography " as search criteria.

offer orders of magnitude higher brilliance with very narrow probe sizes, which in the case of $He^+$ FIB reach even sub-nm dimensions [22], therefore reconciling high milling rates with nm imaging resolution in FIB-SEM tomography experiments. Fig. 2 shows the results for simulations of the interaction between $He^+$ and $Ne^+$ GIS as well as $Ga^+$ LIMS FIB with a common bulk molybdenum specimen at a constant acceleration energy of 40 kV [23]. As observed from the size and shape of the interaction volumes, lighter ions originating from gaseous sources display much higher penetration depths with lower scattering widths, which explain the higher milling power with greater spatial resolution offered by these sources. On the contrary, heavier $Ga^+$ ions emerging from the corresponding liquid source show lower interaction volumes and significant (back)scattering once in contact with the solid specimen. The beneficial traits of GIS make them particularly ideal for FIB-SEM tomography work, and this has spurred their introduction in dual-beam systems. At present, several commercially available instruments, e.g. from Zeiss and ThermoFischer, incorporate multiple GIS, alternatively in combination to a $Ga^+$ LMIS. Thus, they offer a versatile array of milling possibilities which can be optimally selected as a function of the specimen, e.g. hard bulk inorganic samples, porous materials, biological samples, etc, and the goal of the FIB experimental work [24].

In a quest for yet higher milling rates, advanced ion sources have been developed in the most recent years. A technology which offers high performance prospects, particularly for FIB-SEM inspection of large material volumes, is the Xe plasma FIB, which was commercially introduced about 10 years ago and has since been installed in several microscopy labs worldwide [25]. Plasma FIB employs inert Xe gas as the milling medium and are capable to operate at currents in the μA range, which result in volumetric material removal rates which are from 5 to several tenfold higher compared to $Ga^+$ FIBs, depending on the specimen composition, enabling faster preparation of imaging blocks of large dimensions. An additional attractive feature of this technology is that the chemical inertness of Xe adds also to lower implantation rates as well as thinner amorphization layers on exposed cross-sections. These advantageous features have contributed to a relatively fast establishment of this technology as a routine milling tool in material sciences, in particular for a high-throughput preparation of ultrathin lamella for TEM. However, plasma sources have typically broader final probe sizes compared to $Ga^+$ LMIS, particularly at low currents. This decreases their appealingness for FIB-SEM tomography tasks whenever milling with sub-100 nm resolution is required to properly resolve e.g sub-μm macropores or large mesopores in catalyst materials.

Very recently, femtosecond pulsed laser ablation has been introduced as a yet more powerful milling approach in dual-beam instruments [26]. While nanosecond lasers have been classically applied for material ablation, their characteristic pulse time enables a noticeable heat transfer to the milled solid, and undesired thermal affects as a consequence. On the contrary, femtosecond pulse lengths deliver a very rapid albeit athermal ablation, which opens the door to milling rates orders of magnitude higher than those within reach with traditional $Ga^+$ LMIS. Recently, dual-beam FIB-SEM commercial instruments incorporating the ultrafast fs-laser ablation in a chamber adjacent to the FIB-SEM instrument have been introduced by the German provider ZEISS [27]. As illustrated in Fig. 3, the milling of extraordinarily large trenches, with hundreds of μm lateral dimensions, on hard specimens is possible within seconds, compared to the several hours ablation time required with $Ga^+$ FIBs. This sets fs-laser milling as a promising method for ultrafast sample pre-conditioning for FIB-SEM tomography, which is expected to reduce data collection to essentially the time required for the sequential FIB-milling/SEM-imaging on the specimen's block of interest.

With regard to the electron column, dual-beam instruments have benefited from the significant progress achieved in high-resolution SEM detectors over the last decades. However, compared to standard SEM, lower degrees of freedom apply to FIB-SEM experiments, e.g. as to the working distance if the sample remains tilted at the coincident point of the ion and electron guns during the *slice & view* collection of a stack of cross-sectional micrographs. Most modern instruments incorporate various SEM detectors. Next to a conventional secondary-electron, e.g. a Everhart-Thornley (ET) detector, in-lens (frequently also referred to as through-the-lens, immersion-lens, or upper) detectors are incorporated within the electron column to collect both primary SE (SE-I) as well as backscattered electrons (BSE). In-lens detectors with annular geometry and located up in the e-column deliver cross-sectional imaging with lower topographic contrast, thus complementing the information retrieved with SE detection [28].

Next to SEM, dual-beam instruments may also be equipped with Electron Backscatter Diffraction detectors (EBSD) and Energy-Dispersive spectroscopy (EDS) detectors which, in combination with sequential cross-section FIB-milling, may be applied to record EBSD and EDS 3D tomograms, respectively. The former delivers information on grain size and relative spatial orientation and is particularly powerful in fields such as metallurgy and geology [29,30]. EDS tomography is potentially highly informative in the area of catalysis, as it delivers 3D compositional information, which is complementary to the structural elucidation by FIB-SEM tomography [31]. However, it is important to consider that larger interaction volumes with the imaged solid may apply at those X-ray incident energies required to excite specific emission lines of certain elements while recording cross-sectional EDS maps [28]. Hence, the spatial resolution of an EDS tomogram may be substantially lower -particularly along $z$ (the milling direction)- compared to the corresponding FIB-SEM tomogram of the same volume, unless the milling thickness and thus the FIB-SEM tomogram resolution are adjusted to meet the pre-determined EDS analysis depth.

## 3. FIB-SEM tomography workflow

Porous materials are the rule rather than the exception in catalysis research. Fig. 4 summarizes the typical workflow for a FIB-SEM tomography experiment of a porous material, be it a solid catalyst or an electrode. For reasons which shall be explained below, the first step for

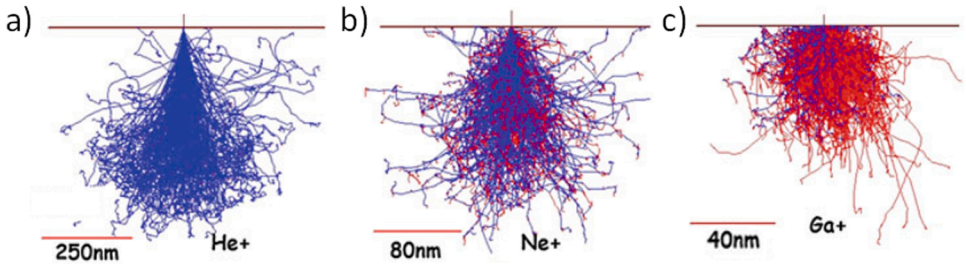


**Fig. 2.** Comparison of shape and size of simulated interaction volumes for a) $He^+$, b) $Ne^+$, and c) $Ga^+$ focused beams of ions in a bulk molybdenum target. The FIB acceleration voltage is 40 kV in all cases. Note the different scale bars.
Adapted with permission from [23].

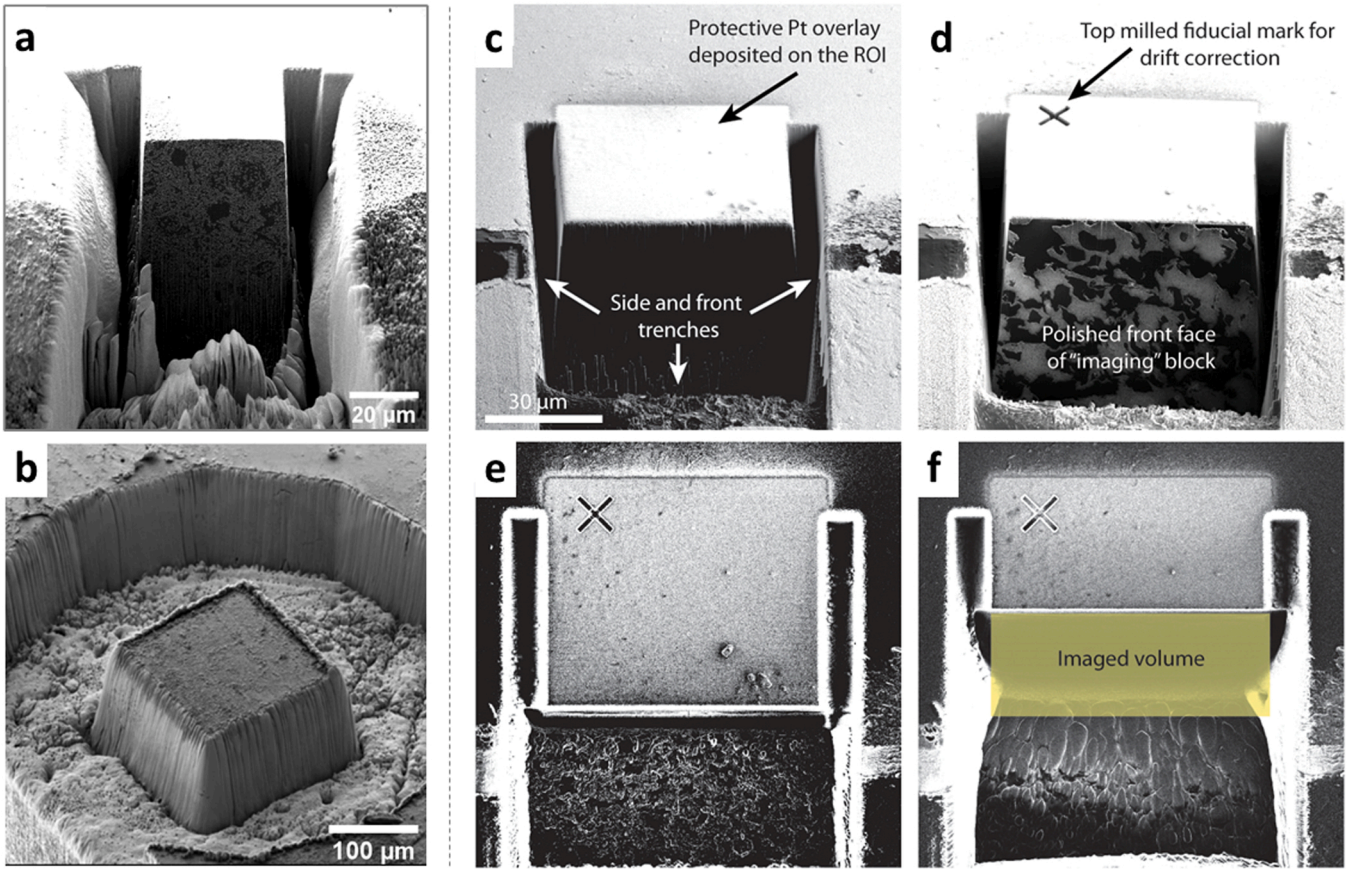


**Fig. 3.** a, b) SEM micrographs of large trenches milled with (a) a $Ga^{+}$ LMIS (ca. 10 h milling time) on the surface of a corundum sample and (b) a femto-pulsed-laser (85 s milling time) on the surface of tungsten carbide. c-f) SEM micrographs of a FIB-SEM imaging block with two lateral and one frontal trench prior to (c-e) and after (f) a slice & image routine in a FIB-SEM tomography experiment on a meso-macroporous $CoRu/Al_2O_3$ catalyst.The volume of sample eroded during the FIB-SEM experiment is marked on panel (f). Panel (b) is reproduced with persmission from [27].

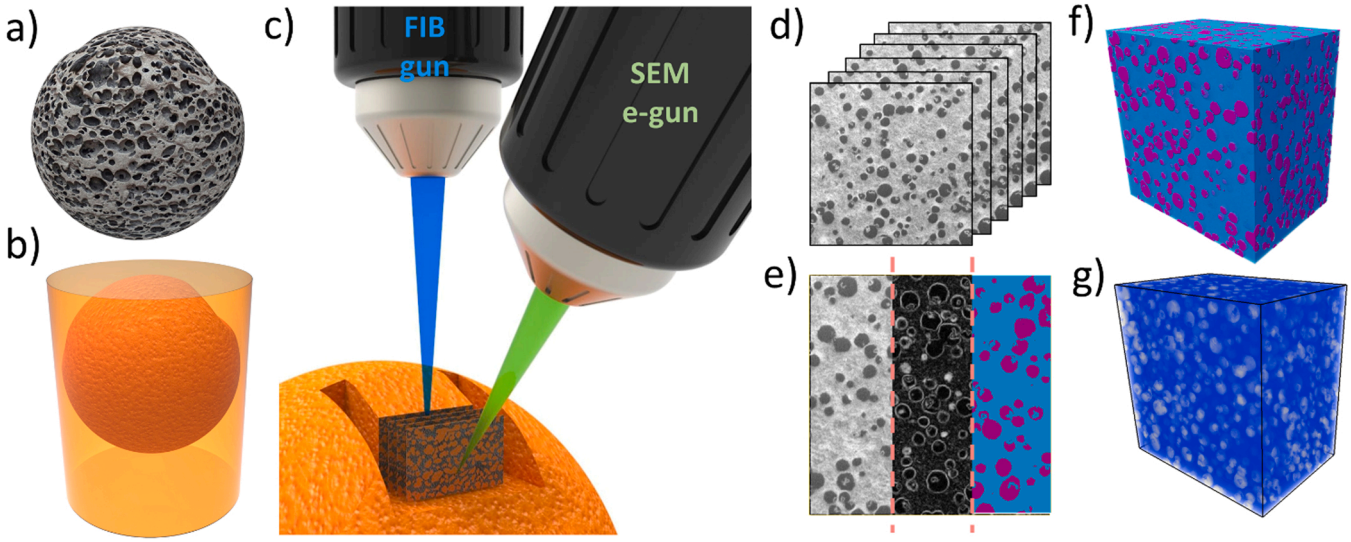


**Fig. 4.** Schematics of the typical workflow for a FIB-SEM tomography experiment on a porous catalyst material. In cronological order: the porous catalyst particle subject of the experiment (a) is embedded in an epoxy resin block ((b), resin displayed in orange color) in order to minimize shine-through artefacts during raw data collection. Following the hardening of the resin and trimming to expose the sample on the outer surface of the block, the sequential *slice & image* experiment is performed in a dual-beam microscope (c). The collection of cross-sectional SEM micrographs (d) is corrected for foreshortening effects and register-aligned to reconstruct the corresponding FIB-SEM tomogram. Matemathical tomogram segmentation enables the classification of individual voxels within the sub-materials contained in the imaged block. Panel (e) shows a 2D illustrative composition with an original SEM micrograph (left) a morphological gradient map generated by a trained watershed algorithm to identify boundaries between different submaterials (center), and the final binarized dataset after segmentation of two submaterials (right), i.e. solid skeleton (cyan color) and pores (magenta color). Panel (f) shows the corresponding segmented tomogram, as a 3D mathematical representation of the volume of material inspected (g) which serves as the input for further 3D image quantification of structural properties.

specimen preparation consists typically of the outgassing of the sample, followed by its embedding in a resin block, normally an epoxy resin. The liquid precursor of the resin material should display the right chemical affinity and viscosity properties to efficiently infiltrate the pore volume of the solid sample. Following the hardening of the resin, the resulting consolidated resin block (Fig. 4b) is typically trimmed, either manually, e.g. using a razor blade, or with the assistance of a pyramitome, a microtome or an ion miller, to ensure that the solid sample becomes exposed on the top surface of the block. Subsequently, the trimmed resin block is mounted on a metallic SEM stub holder, usually followed by metal or carbon sputter coating to create adequate electrical contacts between the sample block and the holder.

Prior to the FIB-SEM experiment, a protective layer of metal is typically deposited on the top surface of the resin block, overcoating the specimen's region of interest (ROI). This overlay provides a uniform first-impact surface for the FIB ions, and minimizes curtaining artefacts (vide infra). Next, a FIB is applied to carve at least one frontal, and often additionally two lateral trenches, thereby defining the block of material to be imaged (Figs. 3 and 4c). These trenches provide access to SEM imaging of the front face of the material's block, as well as wide transport paths around the imaging block to prevent local re-deposition of material — emitted during cross-sectional milling — at locations which obstruct the SEM view on the block's cross-section. Additionally, it is customary to mill at least one fiducial marker near the block's top surface. This marker is fed as a static reference into automated pattern recognition algorithms implemented for an unsupervised adjustment, with nm-precision, of the coordinates for the FIB and SEM guns, in the course of the subsequent *slice & imaging* experiment. Such automated compensation corrects for any unintentional drift of the sample which could bring about deviations in the actual FIB milling work with respect to the pre-established spatial milling pattern, distorting the outcome of the experiment.

Following the preparative milling, the FIB gun is focused onto a finer probe and the front surface of the block is mill-polished until exposure of the sample's cross-section features. Then a *slice & image* algorithm is launched, wherein nm-thick slices of material are removed with the FIB from the front face of the imaging block and the freshly exposed cross-sections are imaged with the SEM (Fig. 4c). The resulting stack of micrographs is corrected for foreshortening effects associated to the angle formed by the SEM gun and the block's cross-sections and aligned, e.g. using cross-correlation algorithms, to reconstruct the corresponding FIB-SEM tomogram (Fig. 4d).

Typically, the first analysis step on the reconstructed tomogram involves morphological segmentation. Segmentation routines determine the boundaries between different sub-materials based on the analysis of the 3D spatial monotony for notions such as discrete voxel intensity (grayscale level), signal regularity, variance, etc, often guided by pre-established similarity criteria. Various segmentation approaches have been developed and applied on reconstructed tomographic volumes of porous catalysts, and they differ in their algorithm implementation, need and use of prior knowledge for sub-materials classification, etc [32]. The outcome from tomogram segmentation is a 3D dataset wherein each voxel has been assigned to a specific sub-material within the imaged volume, defining the boundaries there between (Fig. 4e). The segmented tomograms provide an excellent basis for further 3D structural quantification (Fig. 4f,g). In the case of porous materials, such structural quantification may typically involve the evaluation of total porosity via the assessment of the volume fraction of the sub-materials assigned to pore space. Additionally, higher-level topological notions such as pore connectivity or geometric tortuosity[33] i.e. the ratio of Geodesic (along pore) over Euclidean (straight) distances across the pore system, may be evaluated, for instance on the basis of morphological *skeletonization* analyses which reduce pore systems to a single-voxel thick cord while retaining topological information [34]. Further, different approaches may be applied to derive Pore Network Models (PNM), i.e. simplified computational proxy models, e.g. built upon the interconnection of (pseudo)spherical pore regions by (pseudo)cylindrical pore throats, which emulate the mass transport properties of the reconstructed porous material over an identical x,y,z extension [35]. An extended discussion of the existing 3D image quantification routines is beyond the scope of the present article and the reader is referred to the references above for further details.

In porous samples, such as those of interest in catalysis, the presence of intraparticle cavities and channels within the solid poses challenges to FIB-SEM tomography experiments, by exacerbating technical artefacts which are inherent to the technique. Some of these technical challenges are briefly discussed below.

### 3.1. Curtaining

The intercalation of solid and void spaces in the direction of the vertical ion beam leads to local differences in hardness and thus in milling rates. These are prone to generate curtaining artefacts, i.e. vertical high-contrast ripples which create a waterfall effect on the cross-sectional SEM micrograph (Fig. 5a). Curtains may be incorrectly identified as needle-shaped objects in subsequent image segmentation analyses of FIB-SEM tomograms, which makes it imperative to eliminate or at least minimize these artefacts. Curtaining may be minimized, e.g. by reducing the milling rate through the adjustment of ion beam energy and current [36]. An additional effective measure to inhibit curtaining relies on the creation of a uniform topmost surface onto the specimen's region-of-interest (ROI), e.g. through the deposition of a protective (carbon, Pt, Au) overlay by a pattern-steered, FIB-assisted chemical vapor deposition [37,38]. If the appearance of curtains on the cross-sectional SEM micrographs turns out to be inevitable, digital image post-treatment of the FIB-SEM stack can also be used to correct these artefacts. Given the consistent vertical directionality of curtaining artefacts, filtering off frequencies with vertical orientation in the Fourier space, or through a combination of wavelet and Fourier transforms [39, 40], is in most cases effective to correct, at least minimize, the effects of curtaining artefacts on tomogram segmentation and analysis (Fig. 5a,b).

### 3.2. Pore shadowing

When cross-sections of porous materials become exposed and polished by a FIB, SEM imaging typically results in the detection of electrons emitted from the internal surface of the pores, i.e. from further inner cross-sections of the imaged block. This results in so-called shine-through artefacts and localized shadowing, which notably complicate further image processing of the micrographs stack. In order to overcome these effects, porous materials may be infiltrated with an epoxy resin which, after hardening, fills the pore system and therefore eliminates the presence of voids during FIB-SEM imaging. Obviously, this approach is effective provided that the resin gains access to the entire porosity of the specimen during infiltration, i.e. the pore system is sufficiently connected as to enable full percolation from the specimens outer surface, and it delivers sufficiently different SEM contrast compared to the skeleton of the porous sample after hardening. Moreover, careful selection of the resin's formulation is critical to achieve optimal surface adherence to the sample's inner surface, thus preventing the formation of intra-sample bubbles which result in undesired voids after hardening.

Particularly in electrocatalytic applications, soft porous materials need to be investigated, e.g. polymer electrolytes, carbon electrodes, etc. The similar chemical composition, and therefore low SEM contrast, between sample and epoxy resins may advice against resin embedding. In these cases, resin compositions based on a heavier element like Si, and thus providing higher e-contrast have been proposed [41]. An alternative approach is in situ metal infiltration via the application of the gas deposition system available in most dual-beam devices (Fig. 5c,d). Eswara-Moorthy et al.[42] showcased this method for porous carbon electrodes and found that an e-beam-assisted Pt deposition was beneficial with respect to the FIB-assisted metal deposition, which is

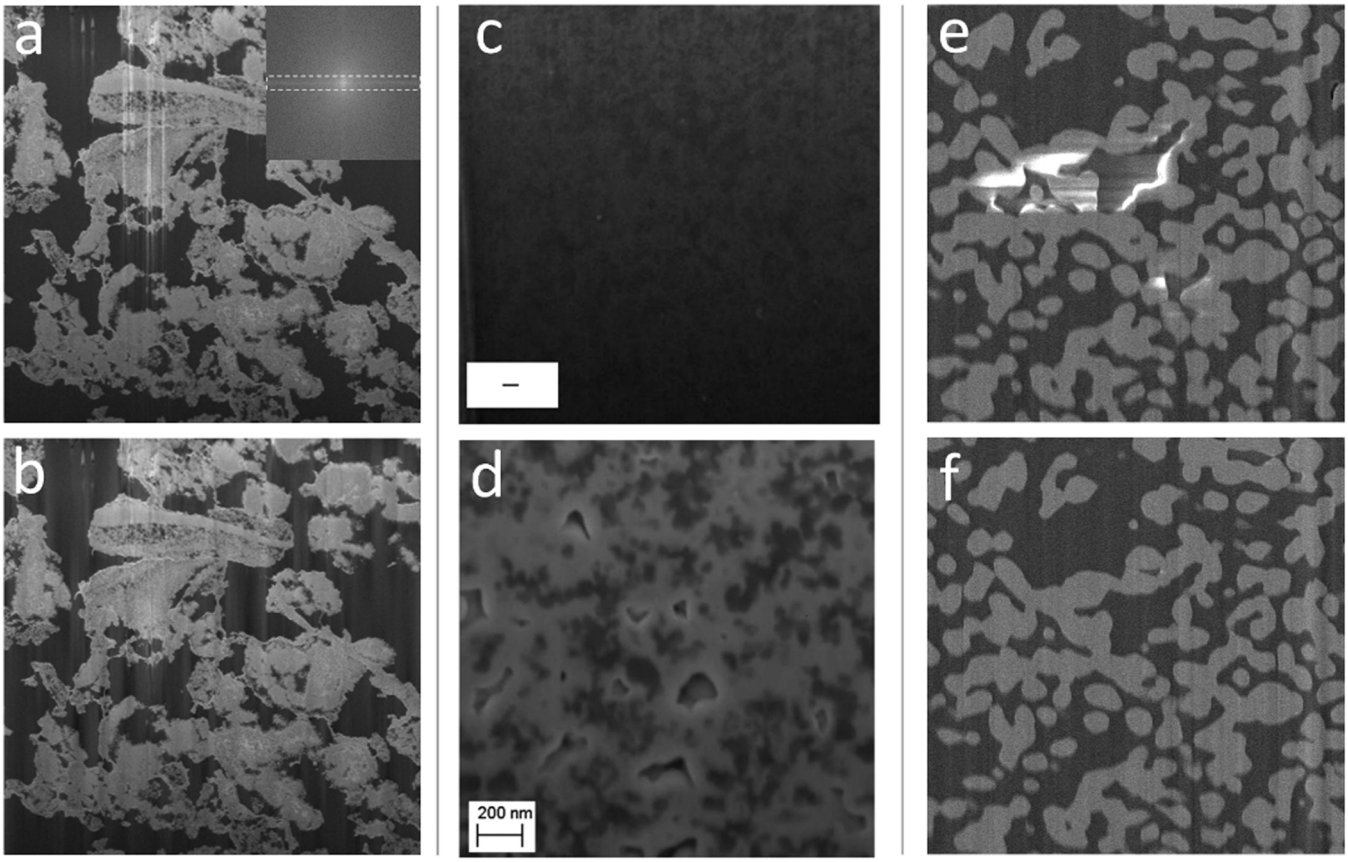


**Fig. 5.** FIB-SEM imaging optimization in porous materials. (a,b) Cross-sectional SEM imaging of a meso-macroporous $Al_2O_3$-based catalyst: a) raw micrograph showing curtaining artefacts and b) after correction of curtaining via a band pass filter in Fourier space. The inset to panel (a) shows the corresponding Fast Fourier Transform (FFT) function for the micrograph, emphasizing the horizontal contributions which correspond to vertically oriented frequencies, including curtaining artefacts, in real space. (c,d) Cross-sectional SEM micrographs of a porous carbon electrode c) vacuum impregnated with a Si-based resin, showing very limited contrast between carbon backbone and resin, and d) pore-filled with Pt (lighter gray regions) via the decomposition of a gaseous Pt organometallic precursor assisted by the electron beam, showing enhanced SEM contrast. Scale bar is 200 nm in both panels (c) and (d). Reproduced with permission from [42], (e,f) Cross-section SEM micrographs of a macroporous $Al_2O_3$ catalyst support registered at two different raster-scan rates, showing its impact on local charging artefacts.

customarily applied for micro fabrications. Electron beam-deposition not only avoided ion implantation and the emergence of structural defects, but it additionally led to orders of magnitude larger deposition depths, which are required to fill the porosity of a sufficiently large volume of the sample. Next to sample infiltration, FIB milling under cryogenic conditions (cryo-FIB) has been proposed to minimize structural damages, material re-distribution and, as a consequence, spurious imaging artefacts when imaging electrodes and catalysts composed of soft polymers and or low-melting point materials [43–45].

If none of the above strategies becomes feasible and the FIB-SEM experiment needs to be run on a void porous material, shine-through artefacts from inner cross-sections become inevitable and a reliable tomogram reconstruction requires from either tedious manual or specific automated post-treatment of the raw cross-sectional SEM micrographs. Terao et al.[46] proposed a reconstruction technique based on the co-registration and matemathical compositation of micrographs using both secondary electrons and energy-selected backscattered (EsB) electrons to identify front-most features. Moroni and Thiele developed an image segmentation routine based on the concept of optical flow, which is designed to discriminate information from further inner cross-sections in FIB-SEM stacks [47].

### 3.3. Local charging

While resin embedding may alleviate pore shadowing effects in porous materials, it also lowers the overall electrical conductivity of the sample. This typically results in local charging at the resin-solid interfaces during cross-sectional SEM imaging, leading to the unsystematic registration of high e-contrast artefacts on the micrographs (Fig. 5e). Charging phenomena may be minimized by optimizing the electron-beam parameters, e.g. applying higher SEM rastering rates over the FIB-exposed cross-sections, and lower e-gun acceleration voltages, typically in the sub-3 kV range (Fig. 5f). When technically possible, the application of electrically conductive resins, which incorporate conductive fillers such as metal colloids or carbon nanostructures, may additionally contribute to a higher overall conductivity and thus lessen charging. Alternatively, localized charge neutralization may be achieved by the injection of nitrogen using a gas injection system [48]. Carbon injection is another effective approach, although the propensity to generate cross-sectioning artefacts advocates to decouple carbon injection from FIB-milling stages in sequential *slice & view* routines [49].

## 4. FIB-SEM tomography in catalysis

### 4.1. Assessment of pore topologies

The kinetics of molecular transport within porous solids is of utmost importance in catalysis, as it determines the accessibility of reactants to the active centers, as well as the average residence time of primary reaction products in contact with catalytic surfaces and therefore the probability to undergo secondary, often undesired, reactions. Pore mass transport in porous catalysts is conventionally modelled via the

effectiveness factor – Thiele modulus correlation [50]. The diffusion coefficient which enters the definition of the Thiele modulus is not the 1st Fick Law molecular diffusion coefficient for unrestricted transport in bulk fluid phases, but rather an *effective* diffusion coefficient after correction by porosity and topological parameters of the porous material within which transport occurs. Such corrections account for the fact that the pore walls represent impermeable barriers for molecular transport.

Pore transport phenomena are also determinant for the overall performance in electrocatalytic applications. In polymer electrolyte fuel cells (PEFC), the realization of higher current densities may become limited by the transport access of oxygen through the gas diffusion and/or catalyst layers at the cathode end [51]. The low operation temperatures of PEFC, and thus intrinsically low gas diffusion coefficients, make the optimization of the pore transport paths essential to avoid oxygen transport bottlenecking performance. Optimization of gas transport rates within the electrodes is also important in solid oxide electrolyte fuel cells (SOEFC) [52].

Traditional porosimetry methods rely on equilibrium phenomena which show a strong dependence on the pore diameter, i.e. capillary condensation in gas physisorption, capillary infiltration in the case of Hg intrusion porosimetry [53], or melting point depression in confinement in the case of water thermoporometry [54,55]. While these methods remain the workhorse of porous materials characterization and deliver statistically significant overall pore size distributions, they face the challenge of assessing parameters of topological nature, i.e. with spatial or directional components, such as pore connectivity [56], pore tortuosity [33], pore constrictivity [57], etc which are highly influential on transport.

In particular, Hg intrusion is the porosimetry method of choice to study macropore networks. Hg intrusion-extrusion isotherms, in combination to the Washburn equation, deliver information on macropore size distributions. However, this analysis inevitably underestimates the pore diameter in pore regions which are only accessible through narrower pore throats. This is exemplified in Fig. 6, with the comparison of the macropore size distributions derived from Hg intrusion porosimetry and FIB-SEM tomography, respectively, for a single porous $BaTiO_3$ ceramic [58]. Moreover, a marked hysteresis, which is often observed between intrusion and extrusion branches, is associated to a combination of factors, including differences in Hg/solid contact angle between the intruding and receding liquid fronts, but also to the so-called *pore network effects*, i.e. a convolution of pore topology factors [59].

Dynamic *controlled-rate* Hg intrusion methods have been developed as an attempt to capitalize the high sensitivity of the method to the narrowest pore throat along the percolation paths [60]. The technique delivers a directional (inwards) radial mapping of the widest pore throat towards any pore volume percolating to the outer surface. This is achieved by detecting fluctuations in the capillary pressure as Hg infiltrates the material at a controlled pace. This way, a certain sense for topological features such as pore constrictivity may be derived. However, the analysis still misses important spatial information, thus providing an incomplete picture of pore architecture and mass transport. As emphasized by Lowell et al. [61] a rigorous reconstruction of a porous material cannot be achieved solely from the analysis of Hg intrusion/extrusion curves. The application of complementary techniques is needed. Direct visualization of macroporous networks with FIB-SEM tomography is a prominent example for such techniques.

Given its spatial resolution, which is limited to ca. $\geq$ 5–10 nm/voxel —mainly owing to the maximum milling precision along the z-direction of the imaged volume—, FIB-SEM tomography is most suited and reliable to investigate macropore networks ($d_p$ >50 nm). However, its application to study pores in the mesopore regime has also been reported. Karwacki et al. [62] studied the introduction of mesoporosity in large ZSM-5 zeolite crystals via steaming treatments, i.e. one of the most widely applied routes to generate intracrystal mesoporosity in zeolites and thus enhance molecular access to acid centers within microporous domains [63]. Voxel dimensions of ca. 5 × 5×10 nm were achieved to visualize mesopores with diameters in the 15–260 nm range. Direct visualization delivered information not only on mesopore size but also 3D distribution and directionality. The results revealed a much higher susceptibility for mesopore formation along the sinusoidal zeolite channels compared to the straight channel system in the three-dimensional MFI zeolite structure, leading to an internal architecture-dependent distribution of mesopores. Moreover, a rather short tortuosity was observed for the mesopores, for which the long axis correlated with the axis of the micropores open to the outer surface in each of the zeolite crystal subunits. This suggested that the removal of the material extracted from the zeolite framework (upon steaming) to the outer crystal surface takes place predominantly through the shortest transport path.

Even in cases where resolution limitations discourage its application to image networks comprising small mesopores, FIB-SEM tomography can deliver topological information of direct significance for mesopore transport processes in hierarchically porous materials, i.e. those integrating various modes of pores extending over different size regimes. Our group has applied FIB-SEM tomography to visualize the internal macroporous architecture in multimodally porous cobalt-based Fischer-Tropsch catalysts which integrate complex and interconnected mesopore and macropore systems [64,65]. Macropore networks could be reconstructed with precision from the corresponding FIB-SEM tomograms. Whilst the resolution of the method was insufficient to directly

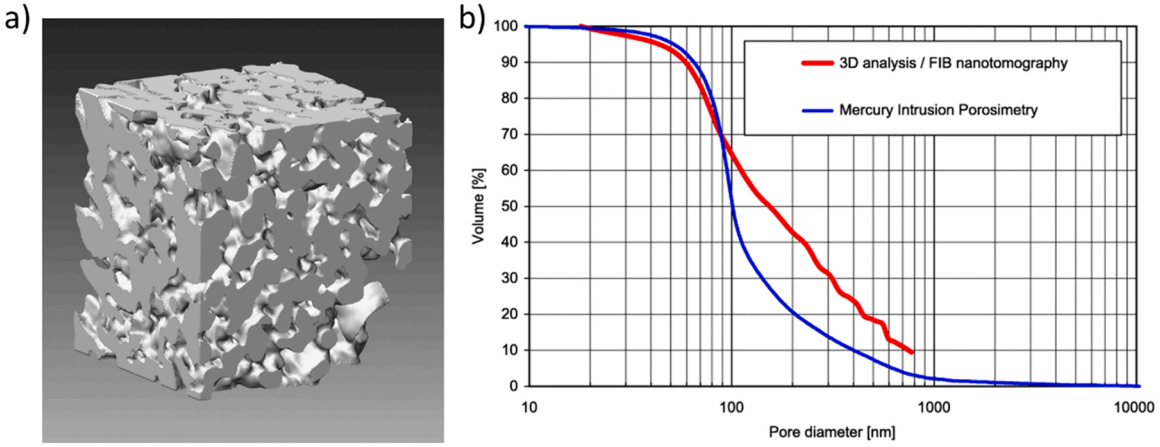


**Fig. 6.** a) Reconstructed FIB-SEM tomogram and, b) comparison of pore size distributions derived from Hg intrusion porosimetry and 3D analysis of the FIB-SEM tomogram for a $BaTiO_3$ ceramic electrode material.
Reproduced with permission from [58].

visualize the mesopores in the samples (ca. 10 nm in diameter), detailed information could be retrieved on the shortest transport distances across mesoporous domains to the nearest intersection with the system of wider macropore openings (Fig. 7). This information was useful to illuminate how a trimodal meso-macro-macroporous architecture could reduce effective mesopore transport distances down to the sub-100 nm range, i.e. more than three orders of magnitude shorter compared to the macroscopic catalyst particle dimensions. The design of hierarchically porous catalysts with greatly reduced mesopore transport distances for primary α-olefin reaction products inhibited secondary olefin hydrogenation reactions, thereby unlocking unconventional reaction product patterns enriched in synthetic linear α-olefins [65].

Often, the bottle neck in research on porous materials with FIB-SEM tomography lies in raw data collection and reconstruction of experimental tomograms. Thus, in certain instances, the combination of experimental and simulated datasets may notably expand the study space. De Winter et al.[66] pursued such a combination of experimental and simulated tomograms to investigate pore transport in different microbead catalyst particles for Fluid Catalytic Cracking (FCC), a process at the root of crude refining and petrochemistry. In FCC, the porosity of the composite catalyst particles, i.e. the void space defined by active zeolite component/s, binders and other ingredients, is influential for the accessibility of bulky hydrocarbon reactants to the active acid sites. Besides, pore transport is also determinant for the intraparticle residence time of primary cracking products and therefore the probability for secondary cracking and coke laydown reactions, which determine the process efficiency and catalyst lifetime. Various cubic volumes (8 $\mu m^3$) were experimentally imaged for particles from two sets of industrially manufactured FCC catalysts. Then, a larger set of virtual volumes were produced via a snake algorithm, to have overall porosities, i.e. fraction of voxels corresponding to pore space, in the range of those determined on the real tomograms. The virtual volumes enabled a larger number of pore transport simulations at notably lower computational cost compared to using only real tomogram reconstructions. Their results depicted the dependence of the pore transport ability (σ), defined as the ratio between unhindered flow over the flow impeded by the specific porous model, with the fraction of connected porosity, i.e. percolating to the outer bounds of each tomogram (Fig. 8). Next, an upscaling routine was implemented, wherein the restriction to mass transport coming from individual, smaller tomographic volumes was integrated, using a model based on the coupling of resistors, to represent pore transport in the integral, larger catalyst microparticles. This approach enabled the researchers to include the contribution from dense "skin" overlays, ascertained in certain technical catalyst formulations [66].

Inoue and Kawase [67] simulated FIB-SEM tomograms for catalyst layers in PEFC. Both the packing of the carbon black backbone, as well as the coating thereof with an ionomer, were considered as variables in the generation of a set of virtual datasets. Comparison to experimental tomograms provided hints as to the interdependence of the effective diffusion coefficient and the total porosity in real systems. Moreover, the analysis of the larger set of numerically generated tomograms emphasized the morphology of the ionomer adhesion and the presence of large isolated pores within the catalyst layer as dominant factors for pore transport and performance.

Extending the study space through the generation of simulated tomograms is also of interest when training segmentation routines based on machine learning concepts. The need for large amounts of accurately segmented tomograms in the training phase establishes a bottle neck for the overall analysis. Fend et al. [68] trained a convolutional neural network (CNN) for the automated segmentation of FIB-SEM tomograms, registered for void porous materials, including corrections for shine-through artefacts. In order to accelerate the training of said CNN, they replaced experimental tomograms by virtual image stacks generated using stochastic germ-grain and random packing algorithms. Finally, the trained algorithm was applied on existing FIB-SEM stacks for $ZrO_2$ and carbon porous samples, showcasing the potential of a hybrid experimental/computational approach to debottleneck FIB-SEM tomography research on catalyst materials.

### 4.2. *Electrode interfacial metrics in electrocatalysis*

Quantifying nano/micro-scale interfaces between different functional components is of importance in different catalysis branches. In heterogeneous catalysis, the boundary area between metallic and oxide nanocrystallites may be determinant for the optimization of promotional

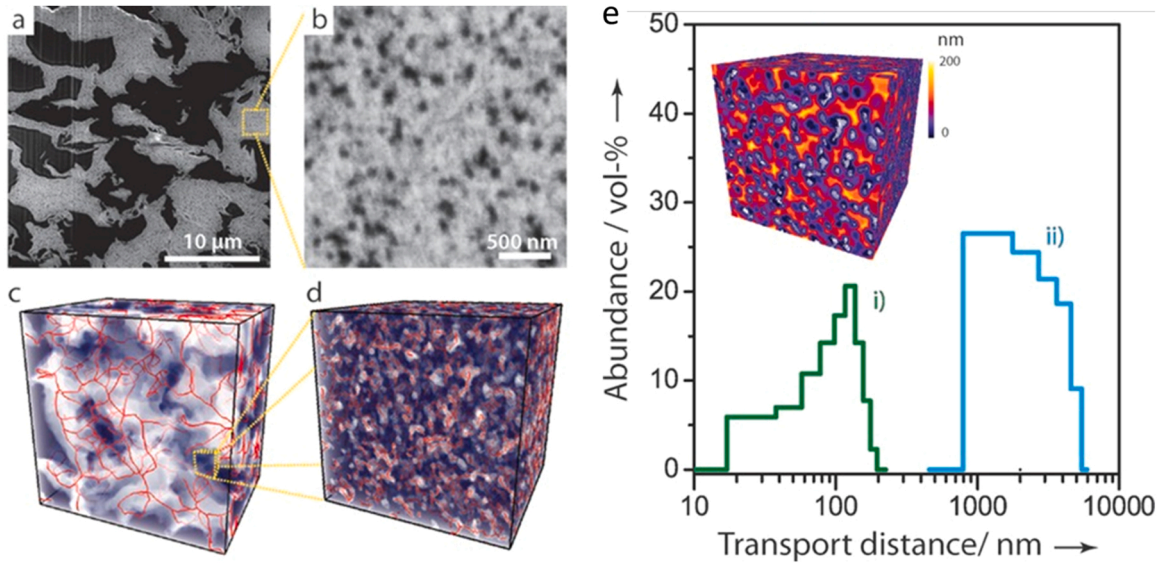


**Fig. 7.** Cross-sectional SEM images (a, b) and reconstructed FIB-SEM tomograms (c, d) showing micrometer- and nanometer-sized macropore systems in a trimodally porous γ-$Al_2O_3$ catalyst support. In (c) and (d), $Al_2O_3$ regions are depicted in blue, and red lines represent the computed macropore skeletons. e)Histograms for the maximum Euclidean distance from mesopore regions to the nanometer (i) and micrometer-sized (ii) macropore systems, respectively, as determined by quantitative 3D image analysis of the FIB-SEM tomograms. The inset shows the 3D-rendered contour map for the Euclidean distance through mesopore regions to the nanometer-sized macropore system, which are relevant for the pore residence time of primary products, and thus the selectivity, in Fischer-Tropsch catalysis.
Adapted with permission from [64].

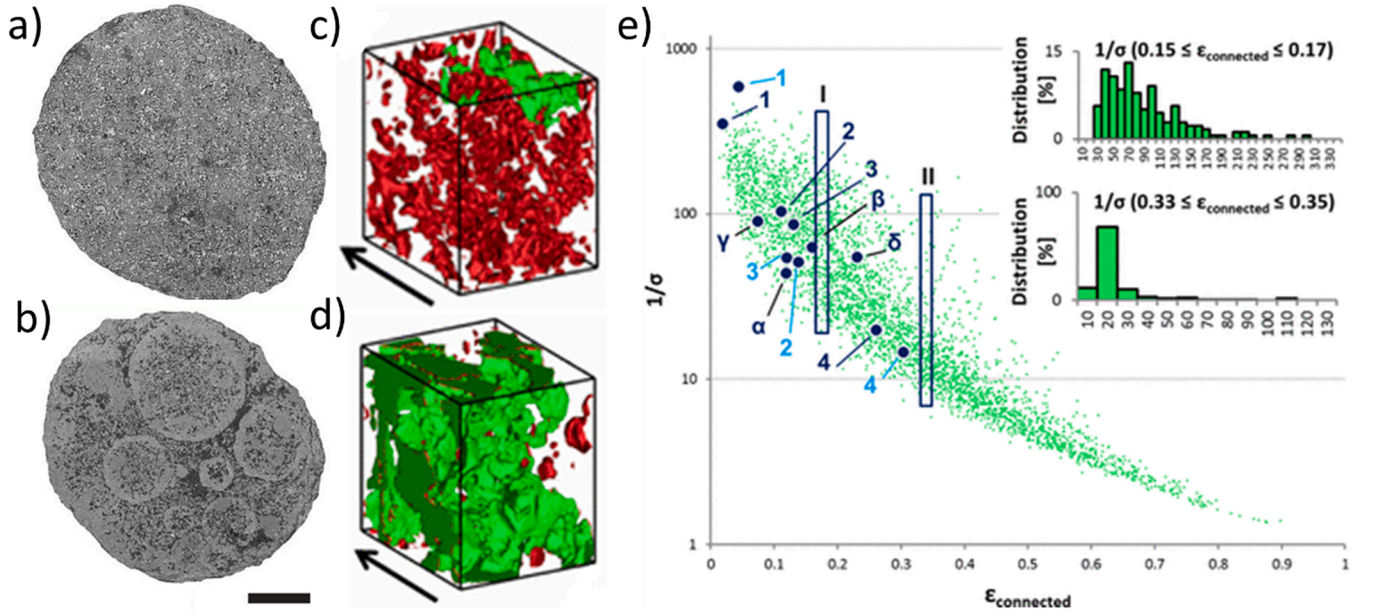


**Fig. 8.** a,b) Cross-sectional SEM micrographs for two types of fluid catalytic cracking (FCC) catalyst microparticles, i.e. FCC1 (a) and FCC2 (b). Scale bar is 25 μm. c, d) Segmented FIB-SEM tomograms, showing connected (percolating) porosity in green and not connected (isolated) porosity in red for cubic subvolumes of $2 \times 2 \times 2$ μm$^3$ of FCC1 (c) and FCC2 (d). e) Scatter plot of the inverse of the transport ability ($\sigma^{-1}$) as a function of the connected porosity (ε) for percolating virtual tomographic volumes generated by a snake algorithm (smaller green scatter symbols) and real FIB-SEM tomographic subvolumes (larger dark blue symbols). The insets show the skewed distribution for specific porosity ranges.
Reproduced with permission from [66].

effects. Determining the extension of functional interfaces is particularly relevant in electrocatalysis. At the anode of SOEFC, the electrode is typically a two-phase porous architecture, wherein so-called triple phase boundaries (TPB) are defined as the junctions between the two solid phases and the pore phase. At TPBs, ions and electrons can be conducted through the ion-conducting and electron-conducting phases, respectively, with concomitant access of gases through the void pore phase. An interrupted percolation of each of these three phases, from TPB to the corresponding sourcing and collection points (electrolyte, current collector, gas supply), is important to design advanced anode ceramics [69].

Doraswami et al. [70] applied FIB-SEM tomography to quantify the TPB uninterrupted length per unit volume in standard Ni/YSZ (yttria-stabilized zirconia) anodes. The values were then used as an input for a 2D distributed finite element model of a hollow fiber SOE fuel cell. For identical TPB distributions, the model predicted a faster electrochemical kinetics to constrain the reaction current to within 20 μm from the anode/solid electrolyte interface, pointing to improvements in surface area, by the creation of smaller pores, as a prime fiber anode design target. Kishimoto et al. [71] used a similar FIB-SEM tomogram analysis approach to underscore the benefits of ceramic electrodes infiltrated with Ni/GDC (gadolinium-doped ceria) with respect to standard electrodes produced by powder sintering routes. The former were found to provide a greater potential to tune metal particle size and electrode porosity, as well as to achieve extended TPB, resulting in improved electrocatalytic performance. The microstructural effects of GDC nanoparticle infiltration onto Ni/YSZ electrodes were also investigated by Wang et al. [72] Analysis of the FIB-SEM tomograms revealed that GDC infiltration diminished the decay in the TPB density over 100 h durability tests, resulting in longer-term stable performances. Nakajo et al. [73] assessed the microstructural evolution of a Ni/YSZ electrode subjected to long-term operations either as a fuel cell's anode or as an electrolyzer's cathode, respectively. While Ni coarsening was observed in either case, in fuel cell operation, a decrease in the extension of TBP was identified as a major degradation pathway. In the electrolyzer configuration, even though local modifications in TBP density were also revealed by the tomographic investigation, Ni depletion close to the YSZ electrolyte was suggested as the most relevant degradation mechanism.

In recent years, solid-oxide co-electrolysis of $CO_2$ and water has emerged as an interesting entry process in the context of power-to-fuels and power-to-chemicals technologies [74]. The e-syngas produced may be valorized, downstream of the electrolyzer, to a number of synthetic energy carriers and platform chemicals such as Fischer-Tropsch paraffinic e-fuels or methanol. Particularly relevant in this context is the inhibition of side reactions at the electrolysis step, such as internal methanation and carbon deposition, which lower syngas production yields and cause electrode fouling, respectively [75]. Given the known activity of Ni nanocrystals to both the Sabatier and Boudouard reactions, responsible for methane production and carbon laydown, respectively, research efforts have placed the spotlight onto the development of innovative Ni-free electrode ceramics. Sciazko et al. [76] have recently applied FIB-SEM tomography to gain nanoscale structural understanding on such an alternative electrode materials, i.e. $La_{0.9}Sr_{0.1}Cr_{0.5}Mn_{0.5}O_{3-\delta}$ (LSCM) composited with GDC (Fig. 9). In particular, they assessed the impact of varying volume fractions of the two components on the electrode microstructure. LSCM stabilized the electrode's structure and prevented stress-induced nano-scale cracks, which were found to form in the vicinity of the electrolyte for GDC-rich compositions and deemed responsible for higher degradation rates. The tomographic structural feedback served as the basis for the optimization of the electrode composition and microstructure. As a result, the performance of a LSCM-GDC electrode manufactured from powders with ca. 100 nm grain size, showed a performance comparable to a conventional Ni/GDC banchmark, which opens excellent prospects for the development of Ni-free electrodes for high-temperature solid-oxide (co) electrolysis applications.

## 5. Conclusions and outlook

Tomographic techniques have swiftly become essential diagnostic tools in catalysis research. Imaging in 3D, at different lengthscales relevant for (electro)catalytic phenomena, is vital to gain access to

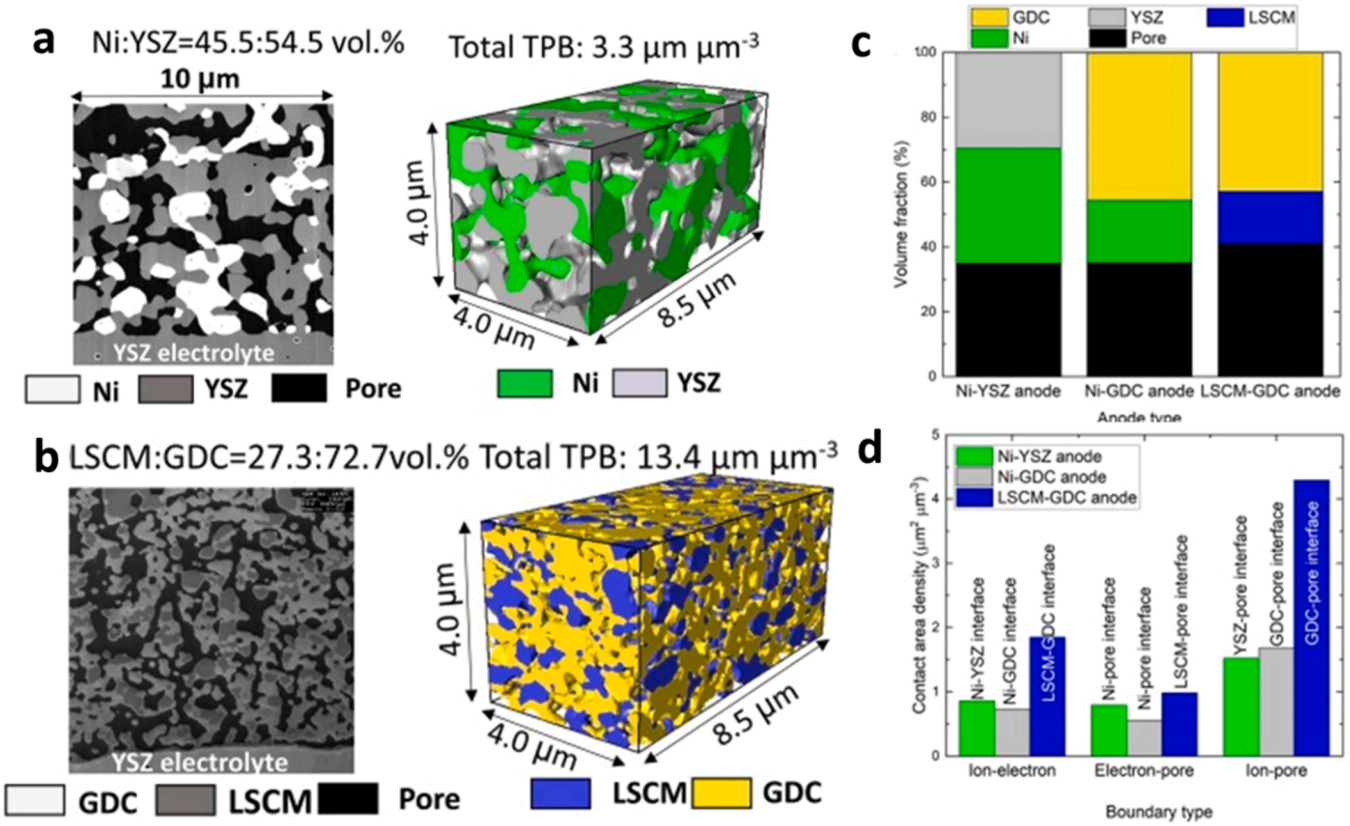


**Fig. 9.** . (a,b) Cross-sectional SEM micrographs and 3D FIB-SEM tomographic reconstructions of a) a conventional Ni-YSZ and b) a Ni-free LSCM-GDC anode catalysts fabricated from standard and nanosized powder precursors, respectively. c) Volume fractions and (d) interphase contact area densities, as determined by 3D image analysis of the FIB-SEM tomograms for said anodes, as well as a Ni-GDC benchmark. YSZ: Yttria-stabilized zirconia; GDC: gadolinium-doped ceria; LSCM: strontium-doped lanthanum chromium manganite.
Adapted with permission from [76].

structural parameters of spatial and topological character, and hence to consider them to make the design of catalyst and electrode materials more rational. FIB-SEM tomography enables the imaging of sample volumes of up to tens of μm lateral dimensions in a single experiment, with down to few nm spatial resolution. Therefore, this technique is particularly attractive to investigate macroporous networks, which are of utmost significance for mass (and charge) transfer phenomena in (electro)catalytic processes.

Recent advances in focused-ion-beams and femto-second pulsed lasers, as well as in secondary/backscattered electron detectors offer prospects for FIB-SEM data collection at increased paces. This shall likely displace the bottleneck of FIB-SEM research to post-processing tasks, related to the reconstruction, de-artefacting and numerical analysis of the corresponding tomograms. With regard to the latter, the development of trainable algorithms based on deep learning concepts, as well as the integration of experimental and simulated tomograms hold the promise for faster and unbiased access to 3D structure-performance relationships. Nevertheless, it behooves scientists and technologists to analyze tomographic data with critical eye and physical sense, as sometimes imperceptible defects e.g. at the stage of unsupervised tomogram segmentation, may translate into sizable flaws when the resulting tomographic segmentations are fed into routines for structure quantification or computational fluid dynamic (CFD) simulations. A rewarding strategy to ensure the reliability of tomographic studies is to benchmark, where possible, local structural data derived from computational image analysis of tomographic reconstructions with “bulk” characterization data provided by physicochemical methods of intrinsically greater sampling. For example, porosity (ε) data may be derived from both voxel counting in FIB-SEM tomograms and a combination of independent measurements of total macropore volume (e.g. by Hg intrusion porosimetry) and skeletal density (e.g. by He picnometry). Grain/nanoparticle size measurements derived from tomographic volumes may be cross-checked with those accessible by methods such as X-ray diffraction or gas chemisorption.

Hitherto, FIB-SEM tomography has proven instrumental to quantify topological parameters in macroporous materials. Access to notions such as pore connectivity, geometrical pore tortuosity, pore constrictivity or transport distances across mesoporous domains in multimodal meso-macroporous catalysts, enables structural descriptions significantly beyond pore size distributions, and of direct significance for the kinetics of pore transport processes. In the field of electrocatalytic applications, access not only to pore topology descriptors, but additionally the capacity to quantify the extent of relevant interfaces, such as triple-phase boundaries of significance for concomitant mass and charge transport phenomena, have been shown to improve the rationale behind the design and development of porous electrode materials with advanced electrocatalytic performance.

Analysis of FIB-SEM tomography data holds the potential to illuminate structural differences between materials for which essentially identical average properties may be determined by more conventional methods, which fall short to assess notions of spatial/topological character. As such, it is envisaged that FIB-SEM tomography will continue to consolidate as a central approach towards the unequivocal description of the internal architecture of catalyst and electrode materials, in relation to their performance, not only in the academic but also in the patent literatures. While applications have thus far been dominated by studies of pore topologies and TPBs in electrocatalysis, the method offers ample possibilities to also quantify, a wider array of micro- and nano-structural

features connected to spatial notions. These include aspects such as co-location patterns or effective distances between constituents within composite materials incorporating various catalytic functionalities, or a combination of catalytic and auxiliary functional (nano)materials, e.g. adsorbents, stimuli “antenna”, selective permeation barriers, etc for tandem/cascade conversion processes and stimuli responsive (electro) catalysis, among other emerging multifunctional applications.

## CRediT authorship contribution statement

**Tania Ródenas**: Conceptualization, Writing – original draft, Project administration. **Gonzalo Prieto**: Conceptualization, Writing – review & editing, Project administration, Supervision, Funding acquisition.

## Declaration of Competing Interest

The authors declare that they have no known competing financial interests or personal relationships that could have appeared to influence the work reported in this paper.

## Data Availability

No data was used for the research described in the article.

## Acknowledgements

Authors acknowledge funding from the European Research Council (ERC-2019-COG 864195, TANDEng). Staff members at the Electron Microscopy Service unit of the UPV are gratefully acknowledged for equipment maintenance and technical assistance.

## References

[1] K.S.W. Singh, J. Rouquerol, G. Bergeret, P. Gallezot, M. Vaarkamp, D. C. Koningsberger, A.K. Datye, J.W. Niemantsverdriet, T. Butz, G. Engelhardt, G. Mestl, H. Knözinger, H. Jobic, Characterization of solid catalysts: sections 3.1.1 – 3.1.3, Handb. Heterog. Catal. (1997) 427–582, https://doi.org/10.1002/9783527619474.ch3a.
[2] P. Felfer, P. Benndorf, A. Masters, T. Maschmeyer, J.M. Cairney, Revealing the distribution of the atoms within individual bimetallic catalyst nanoparticles, Angew. Chem. Int. Ed. 53 (2014) 11190–11193, https://doi.org/10.1002/anie.201405043.
[3] T. Li, P.A.J. Bagot, E. Christian, B.R.C. Theobald, J.D.B. Sharman, D. Ozkaya, M. P. Moody, S.C.E. Tsang, G.D.W. Smith, Atomic imaging of carbon-supported Pt, Pt/Co, and Ir@Pt nanocatalysts by atom-probe tomography, ACS Catal. 4 (2014) 695–702, https://doi.org/10.1021/cs401117e.
[4] J. Zečević, K.P. de Jong, P.E. de Jongh, Progress in electron tomography to assess the 3D nanostructure of catalysts, Curr. Opin. Solid State Mater. Sci. 17 (2013) 115–125, https://doi.org/10.1016/j.cossms.2013.04.002.
[5] R. Leary, P.A. Midgley, J.M. Thomas, Recent advances in the application of electron tomography to materials chemistry, Acc. Chem. Res. 45 (2012) 1782–1791, https://doi.org/10.1021/ar3001102.
[6] E.P.W. Ward, T.J.V. Yates, J.-J. Fernández, D.E.W. Vaughan, P.A. Midgley, Three-dimensional nanoparticle distribution and local curvature of heterogeneous catalysts revealed by electron tomography, J. Phys. Chem. C. 111 (2007) 11501–11505, https://doi.org/10.1021/jp072441b.
[7] J.-P. Tessonnier, O. Ersen, G. Weinberg, C. Pham-Huu, D.S. Su, R. Schlögl, Selective deposition of metal nanoparticles inside or outside multiwalled carbon nanotubes, ACS Nano 3 (2009) 2081–2089, https://doi.org/10.1021/nn900647q.
[8] G. Prieto, J. Zečević, H. Friedrich, K.P. de Jong, P.E. de Jongh, Towards stable catalysts by controlling collective properties of supported metal nanoparticles, Nat. Mater. 12 (2012) 34, https://doi.org/10.1038/nmat3471https://www.nature.com/articles/nmat3471#supplementary-information.
[9] C.J. Gommes, G. Prieto, J. Zecevic, M. Vanhalle, B. Goderis, K.P. de Jong, P.E. de Jongh, Mesoscale characterization of nanoparticles distribution using X-ray scattering, Angew. Chem. Int. Ed. 54 (2015) 11804–11808, https://doi.org/10.1002/anie.201505359.
[10] J. Zečević, C.J. Gommes, H. Friedrich, P.E. de Jongh, K.P. de Jong, Mesoporosity of zeolite Y: quantitative three-dimensional study by image analysis of electron tomograms, Angew. Chem. Int. Ed. 51 (2012) 4213–4217, https://doi.org/10.1002/anie.201200317.
[11] L. Vásárhelyi, Z. Kónya, Á. Kukovecz, R. Vajtai, Microcomputed tomography–based characterization of advanced materials: a review, Mater. Today Adv. 8 (2020), 100084, https://doi.org/10.1016/j.mtadv.2020.100084.
[12] J. Kim, V. Nese, J. Joos, K. Jeske, N. Duyckaerts, N. Pfänder, G. Prieto, Directional freeze-cast hybrid-backbone meso-macroporous bodies as micromonolith catalysts for gas-to-liquid processes, J. Mater. Chem. A 6 (2018) 21978–21989, https://doi.org/10.1039/C8TA07512C.
[13] J. Becher, T.L. Sheppard, Y. Fam, S. Baier, W. Wang, D. Wang, S. Kulkarni, T. F. Keller, M. Lyubomirskiy, D. Brueckner, M. Kahnt, A. Schropp, C.G. Schroer, J.-D. Grunwaldt, Mapping the pore architecture of structured catalyst monoliths from nanometer to centimeter scale with electron and X-ray tomographies, J. Phys. Chem. C 123 (2019) 25197–25208, https://doi.org/10.1021/acs.jpcc.9b06541.
[14] S. Gao, P. Wang, F. Zhang, G.T. Martinez, P.D. Nellist, X. Pan, A.I. Kirkland, Electron ptychographic microscopy for three-dimensional imaging, Nat. Commun. 8 (2017) 163, https://doi.org/10.1038/s41467-017-00150-1.
[15] F. Pfeiffer, X-ray ptychography, Nat. Photonics 12 (2018) 9–17, https://doi.org/10.1038/s41566-017-0072-5.
[16] A.M. Wise, J.N. Weker, S. Kalirai, M. Farmand, D.A. Shapiro, F. Meirer, B. M. Weckhuysen, Nanoscale chemical imaging of an individual catalyst particle with soft X-ray ptychography, ACS Catal. 6 (2016) 2178–2181, https://doi.org/10.1021/acscatal.6b00221.
[17] S. Baier, C.D. Damsgaard, M. Scholz, F. Benzi, A. Rochet, R. Hoppe, T. Scherer, J. Shi, A. Wittstock, B. Weinhausen, J.B. Wagner, C.G. Schroer, J.-D. Grunwaldt, In situ ptychography of heterogeneous catalysts using hard X-rays: high resolution imaging at ambient pressure and elevated temperature, Microsc. Microanal. 22 (2016) 178–188, https://doi.org/10.1017/S1431927615015573.
[18] L. Holzer, M. Cantoni, Review of FIB-tomography, in: nanofabrication using focus, Ion. Electron Beams Princ. Appl. (2012) 410–435.
[19] R.L. Seliger, R.L. Kubena, R.D. Olney, J.W. Ward, V. Wang, High-resolution, ion-beam processes for microstructure fabrication, J. Vac. Sci. Technol. 16 (1979) 1610–1612, https://doi.org/10.1116/1.570253.
[20] R.J. Young, M.V. Moore, in: L.A. Giannuzzi, F.A. Stevie (Eds.), Dual-Beam (FIB-SEM) Systems BT - Introduction to Focused Ion Beams: Instrumentation, Theory, Techniques and Practice, Springer, US, Boston, MA, 2005, pp. 247–268, https://doi.org/10.1007/0-387-23313-X_12.
[21] N.S. Smith, J.A. Notte, A.V. Steele, Advances in source technology for focused ion beam instruments, MRS Bull. 39 (2014) 329–335, https://doi.org/10.1557/mrs.2014.53.
[22] J. Morgan, J. Notte, R. Hill, B. Ward, An introduction to the helium ion microscope, Micros. Today 14 (2006) 24–31, https://doi.org/10.1017/S1551929500050240.
[23] D.C. Joy, in: D.C. Joy (Ed.), Ion–Solid Interactions and Image Formation BT - Helium Ion Microscopy: Principles and Applications, Springer, New York, New York, NY, 2013, pp. 17–37, https://doi.org/10.1007/978-1-4614-8660-2_4.
[24] J. Wang, S. Randolph, Q. Wu, A. Botman, J. Schardt, C. Bouchet-Marquis, X. Nan, C. Rue, M. Straw, Reactive oxygen FIB spin milling enables correlative workflow for 3D super-resolution light microscopy and serial FIB/SEM of cultured cells, Sci. Rep. 11 (2021) 13162, https://doi.org/10.1038/s41598-021-92608-y.
[25] T.L. Burnett, R. Kelley, B. Winiarski, L. Contreras, M. Daly, A. Gholinia, M. G. Burke, P.J. Withers, Large volume serial section tomography by Xe plasma FIB dual beam microscopy, Ultramicroscopy 161 (2016) 119–129, https://doi.org/10.1016/j.ultramic.2015.11.001.
[26] M.P. Echlin, A.T. Polonsky, J. Lamb, R. Geurts, S.J. Randolph, A. Botman, T. M. Pollock, Recent developments in femtosecond laser-enabled TriBeam systems, JOM 73 (2021) 4258–4269, https://doi.org/10.1007/s11837-021-04919-0.
[27] B. Tordoff, C. Hartfield, A.J. Holwell, S. Hiller, M. Kaestner, S. Kelly, J. Lee, S. Müller, F. Perez-Willard, T. Volkenandt, R. White, T. Rodgers, The LaserFIB: new application opportunities combining a high-performance FIB-SEM with femtosecond laser processing in an integrated second chamber, Appl. Microsc. 50 (2020) 24, https://doi.org/10.1186/s42649-020-00044-5.
[28] M. Cantoni, L. Holzer, Advances in 3D focused ion beam tomography, MRS Bull. 39 (2014) 354–360, https://doi.org/10.1557/mrs.2014.54.
[29] D. Dingley, Progressive steps in the development of electron backscatter diffraction and orientation imaging microscopy, J. Microsc. 213 (2004) 214–224, https://doi.org/10.1111/j.0022-2720.2004.01321.x.
[30] W. Xu, M. Ferry, N. Mateescu, J.M. Cairney, F.J. Humphreys, Techniques for generating 3-D EBSD microstructures by FIB tomography, Mater. Charact. 58 (2007) 961–967, https://doi.org/10.1016/j.matchar.2006.10.001.
[31] G.D. WEST, R.C. THOMSON, Combined EBSD/EDS tomography in a dual-beam FIB/FEG–SEM, J. Microsc. 233 (2009) 442–450, https://doi.org/10.1111/j.1365-2818.2009.03138.x.
[32] L.E. Carvalho, A.C. Sobieranski, A. von Wangenheim, 3D segmentation algorithms for computerized tomographic imaging: a systematic literature review, J. Digit. Imaging 31 (2018) 799–850, https://doi.org/10.1007/s10278-018-0101-z.
[33] B. Ghanbarian, A.G. Hunt, R.P. Ewing, M. Sahimi, Tortuosity in porous media: a critical review, Soil Sci. Soc. Am. J. 77 (2013) 1461–1477, https://doi.org/10.2136/sssaj2012.0435.
[34] P.K. Saha, G. Borgefors, G. Sanniti di Baja, A survey on skeletonization algorithms and their applications, Pattern Recognit. Lett. 76 (2016) 3–12, https://doi.org/10.1016/j.patrec.2015.04.006.
[35] Q. Xiong, T.G. Baychev, A.P. Jivkov, Review of pore network modelling of porous media: experimental characterisations, network constructions and applications to reactive transport, J. Contam. Hydrol. 192 (2016) 101–117, https://doi.org/10.1016/j.jconhyd.2016.07.002.
[36] L.A. Giannuzzi Stevie, F. A, Introduction to Focused Ion Beams: Instrumentation, Theory, Techniques, and Practice, Springer, New York, 2005.
[37] P.A. Walley, M. Wineberg, M.S.J. Burden, The use of an electron beam evaporation source for electron microscope sample preparation, J. Phys. E 4 (1971) 501–504, https://doi.org/10.1088/0022-3735/4/7/005.
[38] M. Honda, M. Tamura, K. Nakao, K. Suzuki, Y. Nakagawa, K. Tomishige, Direct cyclic carbonate synthesis from $CO_2$ and diol over carboxylation/hydration cascade

catalyst of CeO2 with 2-cyanopyridine, ACS Catal. 4 (2014) 1893–1896, https://doi.org/10.1021/cs500301d.
[39] M.J. Blunt, B. Bijeljic, H. Dong, O. Gharbi, S. Iglauer, P. Mostaghimi, A. Paluszny, C. Pentland, Pore-scale imaging and modelling, Adv. Water Resour. 51 (2013) 197–216, https://doi.org/10.1016/j.advwatres.2012.03.003.
[40] B. Münch, P. Trtik, F. Marone, M. Stampanoni, Stripe and ring artifact removal with combined wavelet — Fourier filtering, Opt. Express 17 (2009) 8567–8591, https://doi.org/10.1364/OE.17.008567.
[41] M. Ender, J. Joos, T. Carraro, E. Ivers-Tiffée, 3D microstructure analysis of a commercial LiFePO4-cathode, ECS Meet. Abstr. MA2011-02 (2011) 1381, https://doi.org/10.1149/ma2011-02/17/1381.
[42] S.K. Eswara-Moorthy, P. Balasubramanian, W. van Mierlo, J. Bernhard, M. Marinaro, M. Wohlfahrt-Mehrens, L. Jörissen, U. Kaiser, An In situ SEM-FIB-based method for contrast enhancement and tomographic reconstruction for structural quantification of porous carbon electrodes, Microsc. Microanal. 20 (2014) 1576–1580, https://doi.org/10.1017/S1431927614012884.
[43] H. Schulenburg, B. Schwanitz, N. Linse, G.G. Scherer, A. Wokaun, J. Krbanjevic, R. Grothausmann, I. Manke, 3D imaging of catalyst support corrosion in polymer electrolyte fuel cells, J. Phys. Chem. C 115 (2011) 14236–14243, https://doi.org/10.1021/jp203016u.
[44] Y. Katayanagi, T. Shimizu, Y. Hashimasa, N. Matsushita, Y. Yamazaki, T. Yamaguchi, Cross-sectional observation of nanostructured catalyst layer of polymer electrolyte fuel cell using FIB/SEM, J. Power Sources 280 (2015) 210–216, https://doi.org/10.1016/j.jpowsour.2015.01.085.
[45] Y. Li, Y. Li, Y. Cui, Catalyst: how Cryo-EM shapes the development of next-generation batteries, Chem 4 (2018) 2250–2252, https://doi.org/10.1016/j.chempr.2018.09.007.
[46] T. Terao, G. Inoue, M. Kawase, N. Kubo, M. Yamaguchi, K. Yokoyama, T. Tokunaga, K. Shinohara, Y. Hara, T. Hara, Development of novel three-dimensional reconstruction method for porous media for polymer electrolyte fuel cells using focused ion beam-scanning electron microscope tomography, J. Power Sources 347 (2017) 108–113, https://doi.org/10.1016/j.jpowsour.2017.02.050.
[47] R. Moroni, S. Thiele, FIB/SEM tomography segmentation by optical flow estimation, Ultramicroscopy 219 (2020), 113090, https://doi.org/10.1016/j.ultramic.2020.113090.
[48] H. Schulz, U. Zeile, J.P. Stodolka, D. Kraft, Advantages of a local charge compensation system for FIB/SEM applications on insulating materials, Microsc. Microanal. 15 (2009) 332–333, https://doi.org/10.1017/S1431927609096639.
[49] C. Fager, M. Röding, A. Olsson, N. Lorén, C. von Corswant, A. Särkkä, E. Olsson, Optimization of FIB–SEM tomography and reconstruction for soft, porous, and poorly conducting materials, Microsc. Microanal. 26 (2020) 837–845, https://doi.org/10.1017/S1431927620001592.
[50] J. Hoogschagen, Diffusion in porous catalysts and adsorbents, Ind. Eng. Chem. 47 (1955) 906–912, https://doi.org/10.1021/ie50545a016.
[51] B. Abderezzak, Introduction to Transfer Phenomena in PEM Fuel Cells, 2019.
[52] P. Singh, N.Q. Minh, Solid oxide fuel cells: technology status, Int. J. Appl. Ceram. Technol. 1 (2004) 5–15, https://doi.org/10.1111/j.1744-7402.2004.tb00149.x.
[53] C. Schlumberger, M. Thommes, Characterization of hierarchically ordered porous materials by physisorption and mercury porosimetry—a tutorial review, Adv. Mater. Interfaces 8 (2021) 2002181, https://doi.org/10.1002/admi.202002181.
[54] J. Riikonen, J. Salonen, V.-P. Lehto, Utilising thermoporometry to obtain new insights into nanostructured materials, J. Therm. Anal. Calorim. 105 (2011) 811–821, https://doi.org/10.1007/s10973-010-1167-0.
[55] T.M. Eggenhuisen, G. Prieto, H. Talsma, K.P. de Jong, P.E. de Jongh, Entrance size analysis of silica materials with cagelike pore structure by thermoporometry, J. Phys. Chem. C 116 (2012) 23383–23393, https://doi.org/10.1021/jp3070213.
[56] F.J. Keil, C. Rieckmann, Optimization of three-dimensional catalyst pore structures (https://doi.org/), Chem. Eng. Sci. 49 (1994) 4811–4822, https://doi.org/10.1016/S0009-2509(05)80061-2.
[57] E.E. Petersen, Diffusion in a pore of varying cross section, AIChE J. 4 (1958) 343–345, https://doi.org/10.1002/aic.690040322.
[58] L. Holzer, F. Indutnyi, P.H. Gasser, B. Münch, M. Wegmann, Three-dimensional analysis of porous BaTiO3 ceramics using FIB nanotomography, J. Microsc. 216 (2004) 84–95, https://doi.org/10.1111/j.0022-2720.2004.01397.x.
[59] S. Lowell, J.E. Shields, M.A. Thomas, M. Thommes, in: S. Lowell, J.E. Shields, M. A. Thomas, M. Thommes (Eds.), Mercury Porosimetry: Non-wetting Liquid Penetration BT - Characterization of Porous Solids and Powders: Surface Area, Pore Size and Density, Springer, Netherlands, Dordrecht, 2004, pp. 157–188, https://doi.org/10.1007/978-1-4020-2303-3_10.
[60] H. Gao, T. Li, L. Yang, Quantitative determination of pore and throat parameters in tight oil reservoir using constant rate mercury intrusion technique, J. Pet. Explor. Prod. Technol. 6 (2016) 309–318, https://doi.org/10.1007/s13202-015-0186-6.
[61] S. Lowell, J. Shields, M. Thomas, M. Thommes, Characterization of porous solids and powders: surface area, Pore Size Density (2006), https://doi.org/10.1007/978-1-4020-2303-3.
[62] L. Karwacki, D.A.M. deWinter, L.R. Aramburo, M.N. Lebbink, J.A. Post, M. R. Drury, B.M. Weckhuysen, Architecture-dependent distribution of mesopores in steamed zeolite crystals as visualized by FIB-SEM tomography, Angew. Chem. Int. Ed. 50 (2011) 1294–1298, https://doi.org/10.1002/anie.201006031.
[63] Y. Tao, H. Kanoh, L. Abrams, K. Kaneko, Mesopore-modified zeolites: preparation, characterization, and applications, Chem. Rev. 106 (2006) 896–910, https://doi.org/10.1021/cr040204o.
[64] N. Duyckaerts, M. Bartsch, I.-T. Trotuş, N. Pfänder, A. Lorke, F. Schüth, G. Prieto, Intermediate product regulation in tandem solid catalysts with multimodal porosity for high-yield synthetic fuel production, Angew. Chem. Int. Ed. 56 (2017) 11480–11484, https://doi.org/10.1002/anie.201705714.
[65] K. Jeske, A.C. Kizilkaya, I. López-Luque, N. Pfänder, M. Bartsch, P. Concepción, G. Prieto, Design of cobalt fischer–tropsch catalysts for the combined production of liquid fuels and olefin chemicals from hydrogen-rich syngas, ACS Catal. 11 (2021) 4784–4798, https://doi.org/10.1021/acscatal.0c05027.
[66] D.A.M. de Winter, F. Meirer, B.M. Weckhuysen, FIB-SEM tomography probes the mesoscale pore space of an individual catalytic cracking particle, ACS Catal. 6 (2016) 3158–3167, https://doi.org/10.1021/acscatal.6b00302.
[67] G. Inoue, M. Kawase, Effect of porous structure of catalyst layer on effective oxygen diffusion coefficient in polymer electrolyte fuel cell, J. Power Sources 327 (2016) 1–10, https://doi.org/10.1016/j.jpowsour.2016.07.037.
[68] C. Fend, A. Moghiseh, C. Redenbach, K. Schladitz, Reconstruction of highly porous structures from FIB-SEM using a deep neural network trained on synthetic images, J. Microsc. 281 (2021) 16–27, https://doi.org/10.1111/jmi.12944.
[69] P.R. Shearing, D.J.L. Brett, N.P. Brandon, Towards intelligent engineering of SOFC electrodes: a review of advanced microstructural characterisation techniques, Int. Mater. Rev. 55 (2010) 347–363, https://doi.org/10.1179/095066010×12777205875679.
[70] U. Doraswami, P. Shearing, N. Droushiotis, K. Li, N.P. Brandon, G.H. Kelsall, Modelling the effects of measured anode triple-phase boundary densities on the performance of micro-tubular hollow fiber SOFCs, Solid State Ion. 192 (2011) 494–500, https://doi.org/10.1016/j.ssi.2009.10.013.
[71] M. Kishimoto, M. Lomberg, E. Ruiz-Trejo, N.P. Brandon, Enhanced triple-phase boundary density in infiltrated electrodes for solid oxide fuel cells demonstrated by high-resolution tomography, J. Power Sources 266 (2014) 291–295, https://doi.org/10.1016/j.jpowsour.2014.05.038.
[72] Y. Wang, X. Lin, L. Zhang, G. Xiao, C. Guan, J. Yang, X. Lv, D. Liu, J.-Q. Wang, Three-dimensional microstructural characterization of solid oxide electrolysis cell with Ce0.8Gd0.2O2-infiltrated Ni/YSZ electrode using focused ion beam-scanning electron microscopy, J. Solid State Electrochem 25 (2021) 1633–1644, https://doi.org/10.1007/s10008-021-04926-w.
[73] A. Nakajo, A.P. Cocco, M.B. DeGostin, P. Burdet, A.A. Peracchio, B.N. Cassenti, M. Cantoni, J. Van herle, W.K.S. Chiu, Evolution of 3-D transport pathways and triple-phase boundaries in the Ni-YSZ hydrogen electrode upon fuel cell or electrolysis cell operation, ECS Trans. 78 (2017) 3205–3215, https://doi.org/10.1149/07801.3205ecst.
[74] Y. Zheng, J. Wang, B. Yu, W. Zhang, J. Chen, J. Qiao, J. Zhang, A review of high temperature co-electrolysis of H2O and $CO_2$ to produce sustainable fuels using solid oxide electrolysis cells (SOECs): advanced materials and technology, Chem. Soc. Rev. 46 (2017) 1427–1463, https://doi.org/10.1039/C6CS00403B.
[75] S.D. Ebbesen, C. Graves, M. Mogensen, Production of synthetic fuels by Co-electrolysis of steam and carbon dioxide, Int. J. Green. Energy 6 (2009) 646–660, https://doi.org/10.1080/15435070903372577.
[76] A. Sciazko, Y. Komatsu, R. Yokoi, T. Shimura, N. Shikazono, Effects of mass fraction of La0.9Sr0.1Cr0.5Mn0.5O3-δ and Gd0.1Ce0.9O2-δ composite anodes for nickel free solid oxide fuel cells, J. Eur. Ceram. Soc. 42 (2022) 1556–1567, https://doi.org/10.1016/j.jeurceramsoc.2021.11.039.
[77] S. Divi, A. Chatterjee, Generalized nano-thermodynamic model for capturing size-dependent surface segregation in multi-metal alloy nanoparticles, RSC Adv. 8 (2018) 10409–10424, https://doi.org/10.1039/C8RA00945G.